


Skyrmion-based chaotic oscillator driven by a constant current

Laichuan Shen  and Ka Shen *

The Center for Advanced Quantum Studies and Department of Physics, Beijing Normal University, Beijing 100875, China and Key Laboratory of Multi-scale Spin Physics, Ministry of Education, Beijing Normal University, Beijing 100875, China

 (Received 14 November 2023; accepted 10 January 2024; published 24 January 2024)

As an intriguing and useful nonlinear behavior, chaos has recently received increasing attentions in the field of spintronics with the aim of designing novel devices for practical applications. In the present work, we demonstrate a chaotic oscillation of a ferrimagnetic skyrmion through numerical simulations. In contrast to the previous proposals of magnetic-soliton-based chaotic oscillators, the chaos of our ferrimagnetic skyrmion is driven solely by a constant current, instead of a time-dependent one. The occurrence of the chaotic oscillation is found to benefit from the strong nonlinearity of the magnetization dynamics in a ferrimagnet with a relatively weak antiferromagnetic exchange coupling and a low magnetic damping. Our results reveal the potentials of ferrimagnetic skyrmion oscillators in studying chaotic physics and related applications.

DOI: [10.1103/PhysRevB.109.014422](https://doi.org/10.1103/PhysRevB.109.014422)

I. INTRODUCTION

Chaos, referred to as the unpredictable long-term behavior in a deterministic system, has remained an active research topic in the fields of mathematics, physics, chemistry, and biology since its discovery in the late nineteenth century [1]. Recently, practical applications of chaotic dynamics, such as random number generator [2], logic gates [3], and weak signal detection [4,5], have been proposed and attracted increasing research interest. As potential candidates for such applications, chaotic spin nanooscillators based on uniform magnetization dynamics [6,7] or the motion of magnetic solitons, such as domain walls [5,8–10], vortices [11–13], and bimerons [14], have been studied.

In general, the realization of a chaotic spin oscillator requires a phase space of at least three dimensions, namely, with three or more individual state variables to describe the dynamics of the system [15,16]. Since the dynamics of a single macrospin in a static field can be described sufficiently by the evolution of two orientation angles, the chaotic behavior in uniform magnetization dynamics is achieved only if additional degrees of freedom are involved by, for instance, applying time-dependent currents [17,18], injecting feedback currents [19,20] or constructing a device with coupled macrospins [21–23]. In the case of magnetic solitons, similarly, extra variables are also commonly introduced through time-dependent currents/fields to trigger chaotic dynamics because the moving status of typical magnetic solitons is usually indicated only by two variables, e.g., the position and the azimuthal angle of textured spins for a one-dimensional domain wall [8–10] and the two-dimensional location of the guiding center for a vortex [11,12]. Interestingly, as reported recently, a large driving current applied to a vortex could successively flip the magnetization at the vortex core, which thus possesses a new degree of freedom and results in chaotic dynamics [13].

An interesting question is then whether it is possible or how to generate a chaotic motion of a magnetic soliton by a constant current without change in its magnetic texture. In this work, we demonstrate the chaotic dynamics of a ferrimagnetic skyrmion under a constant driving current, by systematically analyzing the spectral function, Lyapunov exponents, and return maps of the skyrmion motion from micromagnetic simulations and the numerical solution of the phenomenological Thiele equation. The occurrence of the chaotic motion is attributed to the expansion of the phase space by including the skyrmion velocity for a comprehensive description of the motion of our massive ferrimagnetic skyrmion. We investigate the dependence of the chaos on different parameters and reveal that a weak exchange coupling between the antiparallelly aligned spin sublattices, which leads to a large effective skyrmion mass, and a low magnetic damping are preferred.

II. MODEL AND METHODS

Figure 1 shows a schematic of our ferrimagnetic skyrmion oscillator with a current injector on top of a synthetic ferrimagnetic working layer. The two ferromagnetic sublayers of the working layer are antiferromagnetically coupled via the Ruderman-Kittel-Kasuya-Yosida (RKKY) interaction [24,25]. The current injector constructed by a spacer and a fixed layer provides current-induced spin transfer torques [26] to trigger the skyrmion dynamics in the working layer.

A. Equation of motion

The motion of the massive ferrimagnetic skyrmion can be derived by the Landau-Lifshitz-Gilbert equation [27] (see Appendix A for the details) and described by the phenomenological Thiele equation [28–31]

$$m_{\text{eff}}\ddot{\mathbf{r}}_c = \mathbf{G} \times \dot{\mathbf{r}}_c - \Gamma\dot{\mathbf{r}}_c + \mathbf{F}_j, \quad (1)$$

where the guiding center of the skyrmion is defined as

$$\mathbf{r}_c = -1/(4\pi Q) \int \mathbf{r}[\mathbf{n} \cdot (\partial_x \mathbf{n} \times \partial_y \mathbf{n})] dx dy, \quad (2)$$

*kashen@bnu.edu.cn

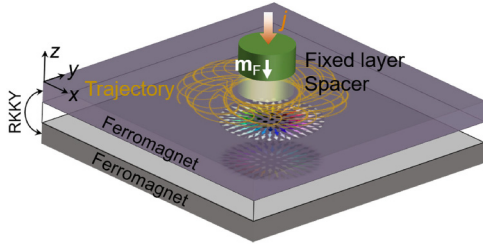


FIG. 1. Sketch of our ferrimagnetic skyrmion oscillator with a synthetic ferrimagnetic working layer and a current injector. The dynamics of the skyrmion in the working layer is driven by the spin-polarized current from the fixed layer of the injector.

with \mathbf{n} being the local Néel vector and the topological charge $Q = -1/(4\pi) \int \mathbf{n} \cdot (\partial_x \mathbf{n} \times \partial_y \mathbf{n}) dx dy$ [32–34]. The effective mass m_{eff} of a symmetric texture in Eq. (1) is expressed as

$$m_{\text{eff}} = (\mu_0 \rho)^2 d_{xx} / (-8J_{\text{RKKY}}), \quad (3)$$

where the structure factor $d_{xx} = \int \partial_x \mathbf{n} \cdot \partial_x \mathbf{n} dx dy$ [35] and the staggered two-dimensional spin density $\rho = t^t M_s^t / \gamma^t + t^b M_s^b / \gamma^b$ with $t^{(b)}$, $M_s^{(b)}$, and $\gamma^{(b)}$ being the thickness, the saturation magnetization, and the gyromagnetic ratio of the top (bottom) sublayer, respectively. Here, μ_0 and J_{RKKY} stand for the vacuum permeability constant and RKKY coupling coefficient, respectively. The first term on the right-hand side of Eq. (1) corresponds to the Magnus force with the gyrovector

$$\mathbf{G} = 4\pi Q \mu_0 \sigma \mathbf{e}_z, \quad (4)$$

which is proportional to the net two-dimensional spin density $\sigma = t^t M_s^t / \gamma^t - t^b M_s^b / \gamma^b$. In the friction term, the dissipation coefficient is expressed as [30]

$$\Gamma = \mu_0 d_{xx} (\alpha^t t^t M_s^t / \gamma^t + \alpha^b t^b M_s^b / \gamma^b), \quad (5)$$

where $\alpha^{(b)}$ is the magnetic damping constant of the top (bottom) sublayer. The last term in Eq. (1) denotes the current-induced driving force

$$\mathbf{F}_j = -(\hbar j P / e) \mathbf{u}, \quad (6)$$

where $u_i = \int_A (\mathbf{n} \times \mathbf{m}_F) \cdot \partial_i \mathbf{n} dx dy$ with the polarization vector \mathbf{m}_F along the $-z$ direction and the subscript A indicating an integral over the area of working layer underneath the current injector. Here, j is the constant intensity of the applied current, \hbar the reduced Planck constant, P the spin polarization efficiency, and e the elementary charge.

Equation (1) can be rewritten into four first-order differential equations of individual variables $(x_1, x_2, x_3, x_4) = (r_{cx}, \dot{r}_{cx}, r_{cy}, \dot{r}_{cy})$,

$$\dot{x}_1 = x_2, \quad (7)$$

$$\dot{x}_2 = -\frac{G}{m_{\text{eff}}} x_4 - \frac{\Gamma}{m_{\text{eff}}} x_2 + \frac{F_{jx}(x_1, x_3)}{m_{\text{eff}}}, \quad (8)$$

$$\dot{x}_3 = x_4, \quad (9)$$

$$\dot{x}_4 = \frac{G}{m_{\text{eff}}} x_2 - \frac{\Gamma}{m_{\text{eff}}} x_4 + \frac{F_{jy}(x_1, x_3)}{m_{\text{eff}}}, \quad (10)$$

which satisfies the prerequisite of chaos in the case where the current-induced force \mathbf{F}_j depends nonlinearly on the skyrmion location \mathbf{r}_c [15].

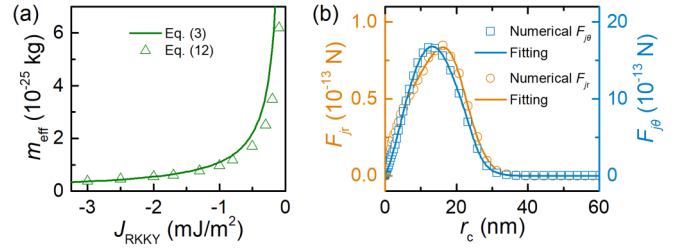


FIG. 2. (a) The effective mass m_{eff} as a function of the RKKY coupling coefficient J_{RKKY} and (b) the radial (F_{jr}) and azimuthal ($F_{j\theta}$) components of the current-induced force as functions of the skyrmion locations (r_c) extracted from micromagnetic simulation. In (a), the curve and the symbols plot Eq. (3) for a static skyrmion with $d_{xx} \approx 18.7$ and Eq. (12) for a moving skyrmion around a circular orbit, respectively. In (b), the symbols and the curves correspond to the plot of Eq. (6) and the fitting from Eq. (13), under the driving current with the diameter of the circular current injector and the current density being $D_j = 30$ nm and $j = 40$ MA/cm², respectively.

To justify the occurrence of the chaos, the Lyapunov exponents of the four variables are defined as [14,18,36]

$$\eta_i = \lim_{t \rightarrow \infty} \frac{1}{t} \ln \frac{\|\delta x_i(t)\|}{\|\delta x_i(0)\|}, \quad (11)$$

where $\|\delta x_i(0)\|$ and $\|\delta x_i(t)\|$ stand for the differences between two simulated trajectories of very close initial state and the values at time t , respectively. The chaotic character is then reflected by the positive value of one or more Lyapunov exponents, which indicates that two trajectories of very close initial conditions will separate exponentially in time and the dynamics become unpredictable.

B. Parameter evaluation

To specify the behavior of the current-induced torque and evaluate the phenomenological parameters, m_{eff} and Γ , in Eq. (1), the spatial distribution of the detailed spin texture is calculated from micromagnetic simulation software MUMAX3 [37]. In the calculation, we introduce the ferrimagnetic nature by using different saturation magnetizations in the two ferromagnetic sublayers and take the geometry and other material parameters identical for both sublayers. Without specified otherwise, the saturation magnetizations of the top and bottom ferromagnets are taken to be $M_s^t = 625$ kA/m and $M_s^b = 580$ kA/m, respectively. The size of each layer is $400 \times 400 \times 1$ nm³ discretized by $1 \times 1 \times 1$ nm³ unit cells. The material parameters fixed in all calculations include the exchange coefficient $A = 15$ pJ/m, the perpendicular magnetocrystalline anisotropy constant $K = 0.8$ MJ/m³, the gyromagnetic ratio $\gamma^t = \gamma^b = 2.211 \times 10^5$ m/(As), the spin polarization efficiency $P = 0.4$, and the Dzyaloshinskii-Moriya exchange coefficient $D = 3.3$ mJ/m² [38].

With the static spin texture obtained from micromagnetic simulation, we obtain $Q = 1$ and $d_{xx} \approx 18.7$, which lead to $G = 3.21 \times 10^{-15}$ kg/s and $\Gamma = 1.28 \times 10^{-15}$ kg/s (with $\alpha = 0.01$), according to Eqs. (4) and (5), respectively. The same d_{xx} also gives the plot of m_{eff} in Eq. (3) as the solid curve in Fig. 2(a). For comparison, one can evaluate the skyrmion mass alternatively by considering the fact that the centripetal

force in a stable circular motion, $m_{\text{eff}}(\dot{r}_c)^2/r_c$, should equal the radial component of the total force, namely,

$$m_{\text{eff}} = -(\mathbf{G} \times \dot{\mathbf{r}}_c + \mathbf{F}_j) \cdot \mathbf{r}_c / \dot{r}_c^2, \quad (12)$$

where the frictional force is discarded due to its vanishing radial component for a circular motion. Note also that the stable circular orbit with different values of J_{RKKY} can be achieved by tuning the damping constant α , which will not affect the spin texture and the effective mass. By using the values of driving force from Eq. (6), we plot Eq. (12) as triangles in Fig. 2(a), which shows a nice agreement with the results from Eq. (3), especially in the strong interlayer coupling regime. The deviation in the weak coupling regime could be attributed to the modification of spin texture due to the presence of driving current.

To capture the skyrmion motion in an arbitrary trajectory, one needs a quantitative description of the relationship between the current-induced force and the skyrmion location. Therefore, we perform a micromagnetic simulation with the ferrimagnetic skyrmion moving in a centrifugal motion defined by a smaller Magnus force with comparable magnetizations of the two sublayers [30], as the change in magnetization only introduces negligible modification in the spin texture. Specifically, we take $M_s^t = 570$ kA/m and $M_s^b = 580$ kA/m. The radial and azimuthal components of the current-induced force from Eq. (6) are plotted in Fig. 2(b) as functions of the skyrmion location. The smaller radial component, compared to the azimuthal one, is because this term comes from the small current-induced modification in the spin texture. For the sake of convenience for further numerical investigation of skyrmion dynamics based on Eq. (1), as shown in Fig. 2(b), the simulated r_c -dependencies of the two current-induced forces are fitted separately by the following expression with the complicated nonlinearity well described

$$F_{jr(j\theta)} = \left(\sum_{n=1}^4 k_n r_c^n \right) / [1 + k_6 \sinh(k_5 r_c)], \quad (13)$$

where k_n are the fitting parameters. Since the current-induced force \mathbf{F}_j is mainly determined by the magnetic texture in the current injection area [see Eq. (6)], the injectors with different shapes and sizes may affect the overlap between the skyrmion texture and the injection area, which will introduce a modification in the dependence of \mathbf{F}_j on the skyrmion location. Specifically, for circular injectors with different diameters, the fitting of the simulated \mathbf{F}_j with Eq. (13) will give different values of the fitting parameters. For the injectors with other shapes, one may need to extend the fitting formula with higher-order r_c -dependence and/or even additional dependence on the azimuthal angle of \mathbf{r}_c .

III. SIMULATION RESULTS

A. Chaotic skyrmion oscillation

The skyrmion trajectories with different values of the RKKY coupling coefficient are simulated by numerically solving the Thiele equation, i.e., Eq. (1). In this simulation, we use the effective mass of a moving skyrmion from Eq. (12), instead of the static mass in Eq. (3), to minimize the unexpected influence. The typical behaviors with a fixed damping

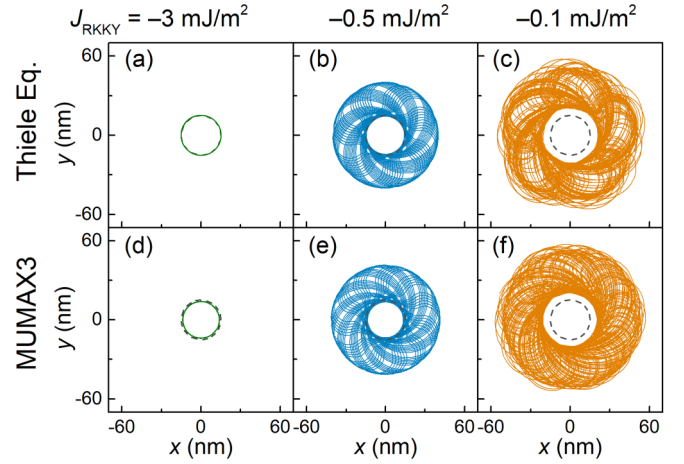


FIG. 3. Trajectories of the skyrmion simulated from (a)–(c) the Thiele equation and (d)–(f) MUMAX3, with different values of RKKY coupling coefficient. Here, we take the damping constant $\alpha = 0.01$, the diameter of the circular current injector $D_j = 30$ nm, and the current density $j = 40$ MA/cm². The dashed circle in each plot stands for the boundary of the current injector.

constant $\alpha = 0.01$ are shown in Figs. 3(a) to 3(c). For the case of a strong RKKY coupling at $J_{\text{RKKY}} = -3$ mJ/m² ($m_{\text{eff}} = 3.71 \times 10^{-26}$ kg) in Fig. 3(a), the skyrmion moves simply around a circular orbit, which is consistent with our previous finding [30]. However, with a weaker RKKY coupling at $J_{\text{RKKY}} = -0.5$ mJ/m² ($m_{\text{eff}} = 1.7 \times 10^{-25}$ kg), the trajectory shown in Fig. 3(b) clearly deviates from the circular motion and presents a regular pattern with its distance to the origin changing with time periodically. Even more interestingly, the skyrmion trajectory in Fig. 3(c) with $J_{\text{RKKY}} = -0.1$ mJ/m² ($m_{\text{eff}} = 6.18 \times 10^{-25}$ kg) does possess a chaotic-type feature without any recognizable regularity. The results from direct micromagnetic simulation with the same parameters are plotted in Figs. 3(d) to 3(f), which show excellent agreements with those from the Thiele equation. In addition, the micromagnetic simulation reveals that, even the weakest RKKY coupling adopted in this work is sufficient to combine the subskyrmions in the two layers, which ensures the validity of the Thiele equation. In the limit of a vanishing RKKY coupling strength, two subskyrmions will become separated and display individual ferromagnetic-skyrmion-type dynamics without chaotic oscillations, where Eq. (1) is no longer applicable.

To understand the skyrmion oscillations beyond a circular motion in Figs. 3(b) and 3(c), we calculate separately the three force terms on the right-hand side of the Thiele equation, Eq. (1). The Magnus force (\mathbf{F}_M), the frictional force (\mathbf{F}_α), and the current-induced force (\mathbf{F}_j) are illustrated by open arrows in orange, green and red colors, respectively, in Fig. 4 for a sequence of skyrmion positions in one period of Fig. 3(b). When the skyrmion approaches the current injection area, the strong current-induced force accelerates the skyrmion to a large velocity so that the Magnus force, which is linear in velocity, is not sufficient to provide the centripetal force required for a stable circular motion of our massive ferrimagnetic skyrmion. As a consequence, the skyrmion experiences a

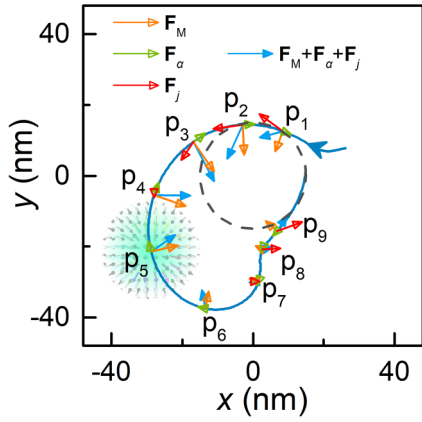


FIG. 4. The force analysis of the skyrmion at different locations within one period of the trajectory in Fig. 3(b). The orange, green, and red open arrows indicate the magnitude and direction of the Magnus force ($\mathbf{F}_M = \mathbf{G} \times \dot{\mathbf{r}}_c$), the frictional force ($\mathbf{F}_\alpha = -\Gamma \dot{\mathbf{r}}_c$) and the current-induced force (\mathbf{F}_j), respectively. The textured spins illustrate the spatial profile of the skyrmion locating at P_5 .

centrifugal motion and gradually leaves the current injection region (see P_1 - P_4). The departure from the injection region suppresses the current-induced force and the Magnus force then becomes dominant and tends to reestablish a circular motion with a radius $r_q = m_{\text{eff}} \dot{r}_c / G$ according to Eq. (12) with $\mathbf{F}_j = 0$. Such a circular motion, however, cannot be sustained, as the skyrmion velocity is reduced by the friction. As seen in Fig. 4, the radius of the orbit gradually decreases from P_4 to P_7 . In the meantime, the skyrmion approaches the injection area again and finally gets overlapped with the injector, which reactivates the driving force. Such processes repeat and result in the skyrmion motion presented in Fig. 3(b). The proper choice of the parameters then drives the system further into a chaotic motion.

To further analyze the characteristic of the skyrmion trajectories, we perform the fast Fourier transformation (FFT) of the x component of \mathbf{r}_c for the three cases in Fig. 3. The corresponding results are plotted in Figs. 5(a) to 5(c). While the regular oscillations in Figs. 3(a) and 3(b) give single- and multi-resonance peaks, respectively, the irregular motion in Fig. 3(c) exhibits a noise-like characteristic in the FFT spectrum as commonly seen in the presence of chaos [39,40].

For a more precise justification of chaotic dynamics, we calculate the Lyapunov exponents from the definition of Eq. (11) and show the convergence of η_i for the three states of skyrmion motion. As shown in Figs. 5(d) and 5(e), none of the Lyapunov exponents are positive for the regular oscillations. In contrast, there is one of the Lyapunov exponents (the red solid curve) keeping positive at long time scale in Fig. 5(f), which indicates clearly the emergence of chaos.

B. Chaos for different values of skyrmion mass and magnetic damping

The above results seem to suggest that a weak interlayer coupling is favored for the realization of chaos. To examine this, we systematically study the skyrmion motion in our ferrimagnetic oscillator by continuously tuning the J_{RKKY} .

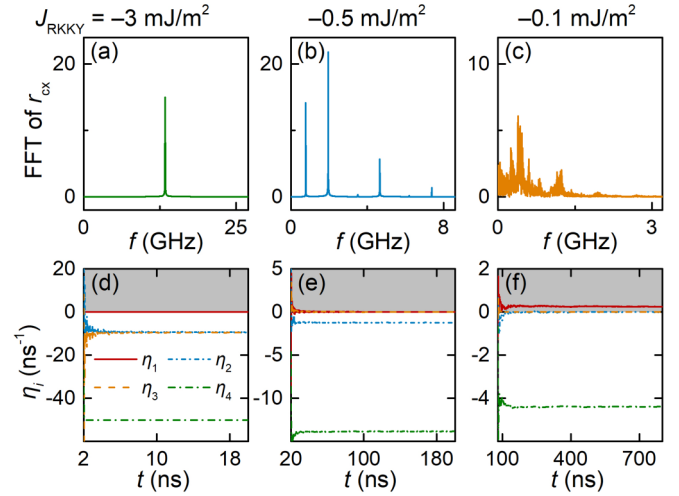


FIG. 5. (a)–(c) FFT spectra of the x component of skyrmion location (r_{cx}) and (d)–(f) convergence plot of Lyapunov exponents η_i for the three skyrmion trajectories in Fig. 3. The gray background indicates the positive values of the vertical axis.

The simulation in this part is carried out through the Thiele equation, where the modulation of J_{RKKY} is equivalent to the change of effective mass, according to Eq. (3). The largest value of the four Lyapunov exponents, i.e., $\eta_{\text{max}} = \max\{\eta_i\}$, is plotted as a function of the effective mass in Fig. 6(a). We see that the positive Lyapunov exponent as a signature of chaos indeed appears mainly in the region of a relatively large skyrmion mass, which corresponds to a weak RKKY coupling [see Fig. 2(a)]. Note also that, instead of continuous parameter region, the appearance of the positive η_{max} is very sensitive to the specific choice of m_{eff} and varies strongly even in the large mass region. This is another common feature for the chaotic behavior [9,11,14,39,41]. Figure 6(b) shows the dependence of η_{max} on the damping constant. As seen, a small damping α promotes the occurrence of chaos, which is similar to the previous finding in bimeron motion [14].

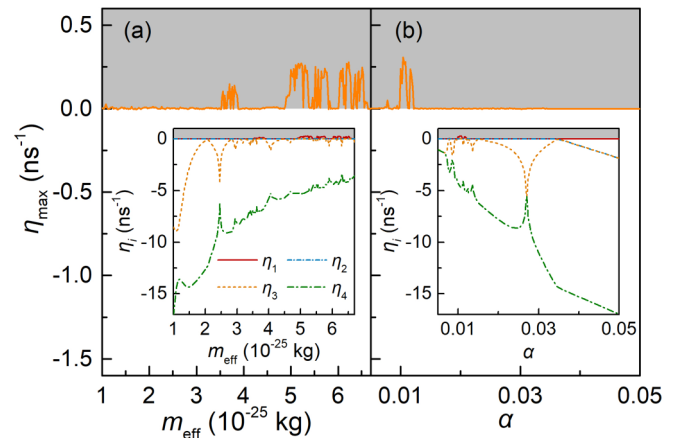


FIG. 6. (a) The largest Lyapunov exponent η_{max} as a function of the skyrmion mass m_{eff} (with $\alpha = 0.01$) and (b) its dependence on the damping constant α (with $m_{\text{eff}} = 6.18 \times 10^{-25}$ kg). The insets show the evolution of η_i .

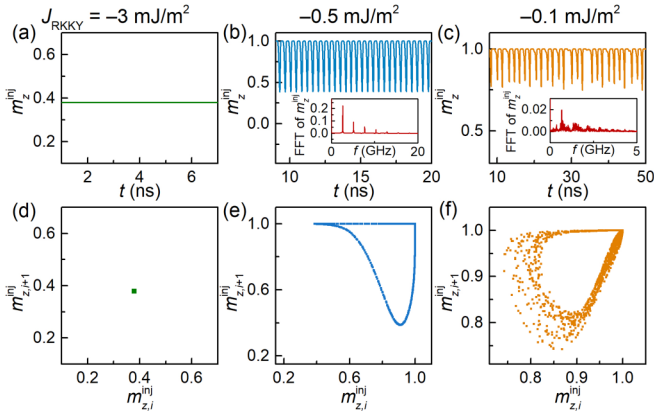


FIG. 7. (a)–(c) The evolution of the recorded magnetizations (m_z^{inj}) with different values of RKKY coupling coefficient. The insets are the FFT spectra of m_z^{inj} . (d)–(f) Corresponding return maps constructed by neighboring sampling points, $m_{z,i}^{\text{inj}}$ and $m_{z,i+1}^{\text{inj}}$, with a temporal interval of 0.1 ns. Here, the adopted parameters are all the same as those used for Fig. 3.

C. Electrical detection of chaotic oscillation

The dynamic behavior of skyrmion motion in nanooscillators can be readout electrically from the magnetoresistance [42,43], which reflects the average magnetization within a detection area. Taking our injector as a detector, the local out-of-plane magnetizations averaged over the ferromagnetic area underneath the injector, m_z^{inj} , are calculated based on the dynamical spin texture from micromagnetic simulations for Figs. 3(d) to 3(f).

As shown in Fig. 7(a), m_z^{inj} is a constant with a value about 0.4 for the skyrmion moving stably along a circular orbit defined by the boundary of the injector. For the multi-frequency regular oscillation in Fig. 3(e), its m_z^{inj} presents a nice periodic evolution in Fig. 7(b), with a frequency comb in its FFT spectrum presented in the inset. Contrarily, the aperiodic characteristics for the chaotic oscillation in Fig. 3(f) are reflected by the time evolution of m_z^{inj} and the noise-like FFT spectrum in Fig. 7(c). This noise-like spectrum is very similar to the FFT spectrum of skyrmion location in Fig. 5(c). Note that the maximum of m_z^{inj} in Figs. 7(b) and 7(c) is close to the ferromagnetic value ($m_z^{\text{inj}} = 1$) because the skyrmion center is already far away from the current injection area, as explained in Fig. 4.

By sampling the m_z^{inj} in Figs. 7(a) to 7(c) at equally spaced intervals and taking two neighboring sampling points $m_{z,i}^{\text{inj}}$ and $m_{z,i+1}^{\text{inj}}$ as the horizontal and vertical axes, respectively, we construct the return maps [44,45] in Figs. 7(d) to 7(f), which exhibit distinct features for the three dynamical phases. While the circular motion gives only a single point in its return map [Fig. 7(d)], the periodic and chaotic oscillations possess a closed loop without and with fluctuation in their return maps, as shown in Figs. 7(e) and 7(f), respectively.

Finally, it is worth pointing out that, although the random force due to the thermal fluctuation can also introduce a similar noise-like spectrum as those in Fig. 5(c) and the inset of Fig. 7(c), the resulting skyrmion trajectory and the

corresponding return map of m_z^{inj} differ qualitatively from the chaotic oscillation. Details of the results are discussed in Appendix B. Note also that the oscillation of skyrmion around the injection area of our oscillator is thanks to the unique ferrimagnetic properties, which is not allowed in skyrmion-based oscillators with an unpatterned working layer of natural/synthetic (anti)ferromagnets [30]. The possibility of constant-current-induced chaos in a confined (anti)ferromagnetic skyrmion oscillator is left for future study.

IV. CONCLUSION

In conclusion, we demonstrated the constant-current-induced chaotic dynamics in a ferrimagnetic skyrmion oscillator by means of the Thiele equation and micromagnetic simulation. The observed chaotic dynamics were further confirmed by the direct calculation of Lyapunov exponents and the spectral function of the oscillation. The distinct behavior of the chaotic oscillator is also analyzed by the return map of the readout of the local magnetization. Our results unravel the rich dynamics of skyrmions in a ferrimagnetic oscillator and provide a promising method to excite chaotic oscillation in spintronics.

ACKNOWLEDGMENTS

This work is supported by the National Natural Science Foundation of China (Grants No. 11974047 and No. 12374100) and the Fundamental Research Funds for the Central Universities.

APPENDIX A: DERIVATION OF THIELE EQUATION

We derive the Thiele equation from the Landau-Lifshitz-Gilbert (LLG) equation of the reduced magnetization (\mathbf{m}^τ) [27]

$$\dot{\mathbf{m}}^\tau = -\gamma^\tau \mathbf{m}^\tau \times \mathbf{H}_{\text{eff}}^\tau + \alpha^\tau \mathbf{m}^\tau \times \dot{\mathbf{m}}^\tau + \gamma^\tau H_j^\tau (\mathbf{m}^\tau \times \mathbf{m}_F) \times \mathbf{m}^\tau, \quad (\text{A1})$$

where the superscript $\tau = t$ (b) for the top (bottom) ferromagnetic sublayer. γ^τ and α^τ are the gyromagnetic ratio and the damping constant, respectively. $\mathbf{H}_{\text{eff}}^\tau$ stands for the effective field

$$\mathbf{H}_{\text{eff}}^{\text{(b)}} = \frac{2J_{\text{RKKY}}}{\mu_0 M_s^{\text{(b)}} t^{\text{(b)}}} \mathbf{m}^{\text{(t)}} + \mathbf{H}_{\text{ex}}^{\text{(b)}} + \mathbf{H}_{\text{an}}^{\text{(b)}} + \mathbf{H}_{\text{DM}}^{\text{(b)}}, \quad (\text{A2})$$

with J_{RKKY} , μ_0 , M_s^τ , and t^τ being the RKKY coupling coefficient, the vacuum permeability constant, the saturation magnetization and the layer thickness, respectively. $\mathbf{H}_{\text{ex}}^\tau$ and $\mathbf{H}_{\text{an}}^\tau$ denote the intralayer exchange field and the magnetic anisotropy field, respectively. The exchange field ($\mathbf{H}_{\text{DM}}^\tau$) from interfacial Dzyaloshinskii-Moriya interaction is described as

$$\mathbf{H}_{\text{DM}}^\tau = \frac{2D^\tau}{\mu_0 M_s^\tau} [\nabla m_z^\tau - (\nabla \cdot \mathbf{m}^\tau) \mathbf{e}_z], \quad (\text{A3})$$

where D^τ is a coefficient and we set $D^t = D^b$ in micromagnetic simulations, which may be achieved, for example, by designing the stacking configuration of multilayer film [46]. In Eq. (A1), \mathbf{m}_F is the polarization vector and $H_j^\tau = j\hbar P / (2\mu_0 e t^\tau M_s^\tau)$ represents the strength of spin transfer

torque, where j , \hbar , P , and e are the current density, the reduced Planck's constant, the spin polarization efficiency, and the elementary charge, respectively.

For the sake of convenience in derivation, Eq. (A1) is rewritten as

$$\frac{t^t M_s^t}{\gamma^t} \dot{\mathbf{m}}^t = -\mathbf{m}^t \times \mathbf{h}_{\text{eff}}^t + \alpha^t \frac{t^t M_s^t}{\gamma^t} \mathbf{m}^t \times \dot{\mathbf{m}}^t + h_j (\mathbf{m}^t \times \mathbf{m}_F) \times \mathbf{m}^t, \quad (\text{A4})$$

$$\frac{t^b M_s^b}{\gamma^b} \dot{\mathbf{m}}^b = -\mathbf{m}^b \times \mathbf{h}_{\text{eff}}^b + \alpha^b \frac{t^b M_s^b}{\gamma^b} \mathbf{m}^b \times \dot{\mathbf{m}}^b + h_j (\mathbf{m}^b \times \mathbf{m}_F) \times \mathbf{m}^b. \quad (\text{A5})$$

Here, $h_j = j\hbar P / (2\mu_0 e)$ and $\mathbf{h}_{\text{eff}}^{(b)} = h_{\text{RKKY}} \mathbf{m}^{b(t)} + \mathbf{h}^{(b)}$ with $h_{\text{RKKY}} = 2J_{\text{RKKY}} / \mu_0$ and $\mathbf{h}^r = (\mathbf{H}_{\text{ex}}^r + \mathbf{H}_{\text{an}}^r + \mathbf{H}_{\text{DM}}^r) M_s^r t^r$. The linear combinations of Eqs. (A4) and (A5) yield the equations of motion for the net magnetization $\mathbf{m} = (\mathbf{m}^t + \mathbf{m}^b) / 2$ and the Néel vector $\mathbf{n} = (\mathbf{m}^t - \mathbf{m}^b) / 2$ as

$$\sigma \dot{\mathbf{m}} + \rho \dot{\mathbf{n}} = -4h_{\text{RKKY}} \mathbf{n} \times \mathbf{m} + \rho_\alpha \mathbf{n} \times \dot{\mathbf{m}} + 2h_j (\mathbf{m} \times \mathbf{m}_F) \times \mathbf{n}, \quad (\text{A6})$$

$$\rho \dot{\mathbf{m}} + \sigma \dot{\mathbf{n}} = -\mathbf{n} \times \mathbf{h}_n + \rho_\alpha \mathbf{n} \times \dot{\mathbf{n}} + 2h_j (\mathbf{n} \times \mathbf{m}_F) \times \mathbf{n}, \quad (\text{A7})$$

where $\sigma = t^t M_s^t / \gamma^t - t^b M_s^b / \gamma^b$ and $\rho = t^t M_s^t / \gamma^t + t^b M_s^b / \gamma^b$. The parameters ρ_α and \mathbf{h}_n are defined as $\rho_\alpha = \alpha^t t^t M_s^t / \gamma^t + \alpha^b t^b M_s^b / \gamma^b$ and $\mathbf{h}_n = \mathbf{h}^t - \mathbf{h}^b$, respectively. According to Eqs. (A6) and (A7) with $|\mathbf{m}| \ll |\mathbf{n}| \sim 1$ in the limit of relatively strong RKKY coupling to make the magnetizations in the two sublayers nearly antiparallel, we derive a closed equation for the Néel vector

$$\frac{\rho^2}{-4h_{\text{RKKY}}} \ddot{\mathbf{n}} \times \mathbf{n} + \sigma \dot{\mathbf{n}} = -\mathbf{n} \times \mathbf{h}_n + \rho_\alpha \mathbf{n} \times \dot{\mathbf{n}} + 2h_j (\mathbf{n} \times \mathbf{m}_F) \times \mathbf{n}. \quad (\text{A8})$$

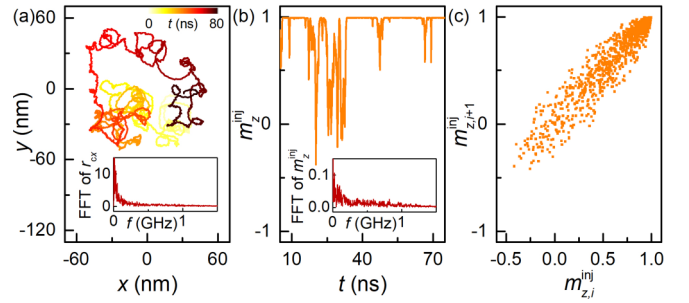


FIG. 8. (a) Trajectory of the skyrmion Brownian motion due to thermal effects at 30 K. The inset shows the FFT spectrum of r_{cx} . (b) The readout of the local magnetization in the injection area from MUMAX3 and (c) the corresponding return map with a temporal interval at 0.1 ns. In this calculation, the size of each ferromagnet is set to be $200 \times 200 \times 1 \text{ nm}^3$ and other parameters are the same as those used for Fig. 3.

Using $\dot{\mathbf{n}} = -(\dot{\mathbf{r}}_c \cdot \nabla) \mathbf{n}$ and $\ddot{\mathbf{n}} = -(\ddot{\mathbf{r}}_c \cdot \nabla) \mathbf{n}$, and spatially integrating the scalar product of Eq. (A8) and $(\mathbf{n} \times \partial_i \mathbf{n})$ [29], one can write out the Thiele equation, Eq. (1). Here, \mathbf{r}_c denotes the skyrmion location.

APPENDIX B: SKYRMION MOTION WITH THERMAL EFFECTS

Figure 8(a) displays the trajectory of the skyrmion in the presence of thermal fluctuation at 30 K, where the thermal effects are introduced by including a stochastic field into the Landau-Lifshitz-Gilbert equation [47]. The thermal-induced Brownian motion of skyrmion is apparently different from the current-induced chaotic oscillation shown in Fig. 3, although the frequency spectra of both cases exhibit similar noise-like characteristics. The time evolution and the return map of the readout from the skyrmion Brownian motion are plotted in Figs. 8(b) and 8(c), which also have different patterns, compared to those of current-induced chaotic dynamics in Figs. 7(c) and 7(f).

- [1] T. Hikihara, P. Holmes, T. Kambe, and G. Rega, Introduction to the focus issue: Fifty years of chaos: Applied and theoretical, *Chaos* **22**, 047501 (2012).
- [2] J. S. Teh, A. Samsudin, M. Al-Mazrooie, and A. Akhavan, GPUs and chaos: A new true random number generator, *Nonlinear Dyn.* **82**, 1913 (2015).
- [3] W. L. Ditto, A. Miliotis, K. Murali, S. Sinha, and M. L. Spano, Chaogates: Morphing logic gates that exploit dynamical patterns, *Chaos* **20**, 037107 (2010).
- [4] G. Wang, D. Chen, J. Lin, and X. Chen, The application of chaotic oscillators to weak signal detection, *IEEE Trans. Ind. Electron.* **46**, 440 (1999).
- [5] L. Shen, J. Xia, M. Ezawa, O. A. Tretiakov, G. Zhao, and Y. Zhou, Signal detection based on the chaotic motion of an antiferromagnetic domain wall, *Appl. Phys. Lett.* **118**, 012402 (2021).
- [6] S. Kaka, M. R. Pufall, W. H. Rippard, T. J. Silva, S. E. Russek, and J. A. Katine, Mutual phase-locking of microwave spin torque nano-oscillators, *Nature (London)* **437**, 389 (2005).
- [7] Z. Zeng, G. Finocchio, and H. Jiang, Spin transfer nano-oscillators, *Nanoscale* **5**, 2219 (2013).
- [8] H. Okuno and T. Homma, Chaotic oscillation of domain wall in non-equilibrium state, *IEEE Trans. Magn.* **29**, 2506 (1993).
- [9] Y. Chen, X. Ge, W. Luo, S. Liang, X. Yang, L. You, Y. Zhang, and Z. Yuan, Chaotic precession of antiferromagnetic domain walls, *Phys. Rev. B* **107**, L020405 (2023).
- [10] A. Pivano and V. O. Dolocan, Chaotic dynamics of magnetic domain walls in nanowires, *Phys. Rev. B* **93**, 144410 (2016).
- [11] A. V. Bondarenko, E. Holmgren, Z. W. Li, B. A. Ivanov, and V. Korenivski, Chaotic dynamics in spin-vortex pairs, *Phys. Rev. B* **99**, 054402 (2019).
- [12] K.-W. Moon, B. S. Chun, W. Kim, Z. Q. Qiu, and C. Hwang, Duffing oscillation-induced reversal of magnetic vortex core by a resonant perpendicular magnetic field, *Sci. Rep.* **4**, 6170 (2014).
- [13] T. Devolder, D. Rontani, S. Petit-Watelot, K. Bouzehouane, S. Andrieu, J. Létang, M.-W. Yoo, J.-P. Adam, C. Chappert, S. Girod, V. Cros, M. Sciamanna, and J.-V. Kim, Chaos in

- magnetic nanocontact vortex oscillators, *Phys. Rev. Lett.* **123**, 147701 (2019).
- [14] L. Shen, J. Xia, X. Zhang, M. Ezawa, O. A. Tretiakov, X. Liu, G. Zhao, and Y. Zhou, Current-induced dynamics and chaos of antiferromagnetic bimerons, *Phys. Rev. Lett.* **124**, 037202 (2020).
- [15] S. Boccaletti, The control of chaos: Theory and applications, *Phys. Rep.* **329**, 103 (2000).
- [16] S. Kumar, X. Wang, J. P. Strachan, Y. Yang, and W. D. Lu, Dynamical memristors for higher-complexity neuromorphic computing, *Nat. Rev. Mater.* **7**, 575 (2022).
- [17] Z. Li, Y. C. Li, and S. Zhang, Dynamic magnetization states of a spin valve in the presence of dc and ac currents: Synchronization, modification, and chaos, *Phys. Rev. B* **74**, 054417 (2006).
- [18] Z. Yang, S. Zhang, and Y. C. Li, Chaotic dynamics of spin-valve oscillators, *Phys. Rev. Lett.* **99**, 134101 (2007).
- [19] T. Taniguchi, N. Akashi, H. Notsu, M. Kimura, H. Tsukahara, and K. Nakajima, Chaos in nanomagnet via feedback current, *Phys. Rev. B* **100**, 174425 (2019).
- [20] J. Williams, A. D. Accioly, D. Rontani, M. Sciamanna, and J.-V. Kim, Chaotic dynamics in a macrospin spin-torque nano-oscillator with delayed feedback, *Appl. Phys. Lett.* **114**, 232405 (2019).
- [21] K. Kudo, R. Sato, and K. Mizushima, Synchronized magnetization oscillations in F/N/F nanopillars, *Jpn. J. Appl. Phys.* **45**, 3869 (2006).
- [22] T. Taniguchi, Synchronized, periodic, and chaotic dynamics in spin torque oscillator with two free layers, *J. Magn. Magn. Mater.* **483**, 281 (2019).
- [23] R. Matsumoto, S. Lequeux, H. Imamura, and J. Grollier, Chaos and relaxation oscillations in spin-torque windmill spiking oscillators, *Phys. Rev. Appl.* **11**, 044093 (2019).
- [24] S. S. P. Parkin, R. Bhadra, and K. P. Roche, Oscillatory magnetic exchange coupling through thin copper layers, *Phys. Rev. Lett.* **66**, 2152 (1991).
- [25] Y. Saito, S. Ikeda, and T. Endoh, Synthetic antiferromagnetic layer based on Pt/Ru/Pt spacer layer with 1.05 nm interlayer exchange oscillation period for spin-orbit torque devices, *Appl. Phys. Lett.* **119**, 142401 (2021).
- [26] J. Slonczewski, Current-driven excitation of magnetic multilayers, *J. Magn. Magn. Mater.* **159**, L1 (1996).
- [27] T. Gilbert, A phenomenological theory of damping in ferromagnetic materials, *IEEE Trans. Magn.* **40**, 3443 (2004).
- [28] A. A. Thiele, Steady-state motion of magnetic domains, *Phys. Rev. Lett.* **30**, 230 (1973).
- [29] S. K. Kim, K.-J. Lee, and Y. Tserkovnyak, Self-focusing skyrmion racetracks in ferrimagnets, *Phys. Rev. B* **95**, 140404(R) (2017).
- [30] L. Shen, Y. Zhou, and K. Shen, Boundary-free spin torque nano-oscillators based on ferrimagnetic skyrmions, *Appl. Phys. Lett.* **121**, 092403 (2022).
- [31] L. Shen, J. Xia, Z. Chen, X. Li, X. Zhang, O. A. Tretiakov, Q. Shao, G. Zhao, X. Liu, M. Ezawa, and Y. Zhou, Nonreciprocal dynamics of ferrimagnetic bimerons, *Phys. Rev. B* **105**, 014422 (2022).
- [32] S.-Z. Lin, A. Saxena, and C. D. Batista, Skyrmion fractionalization and merons in chiral magnets with easy-plane anisotropy, *Phys. Rev. B* **91**, 224407 (2015).
- [33] J. Barker and O. A. Tretiakov, Static and dynamical properties of antiferromagnetic skyrmions in the presence of applied current and temperature, *Phys. Rev. Lett.* **116**, 147203 (2016).
- [34] J. Tang, Y. Wu, W. Wang, L. Kong, B. Lv, W. Wei, J. Zang, M. Tian, and H. Du, Magnetic skyrmion bundles and their current-driven dynamics, *Nat. Nanotechnol.* **16**, 1086 (2021).
- [35] R. Tomasello, E. Martinez, R. Zivieri, L. Torres, M. Carpentieri, and G. Finocchio, A strategy for the design of skyrmion race-track memories, *Sci. Rep.* **4**, 6784 (2014).
- [36] S. De Souza-Machado, R. W. Rollins, D. T. Jacobs, and J. L. Hartman, Studying chaotic systems using microcomputer simulations and Lyapunov exponents, *Am. J. Phys.* **58**, 321 (1990).
- [37] A. Vansteenkiste, J. Leliaert, M. Dvornik, M. Helsen, F. Garcia-Sanchez, and B. Van Waeyenberge, The design and verification of MuMax3, *AIP Adv.* **4**, 107133 (2014).
- [38] J. Sampaio, V. Cros, S. Rohart, A. Thiaville, and A. Fert, Nucleation, stability and current-induced motion of isolated magnetic skyrmions in nanostructures, *Nat. Nanotechnol.* **8**, 839 (2013).
- [39] T. Yamaguchi, N. Akashi, K. Nakajima, S. Tsunegi, H. Kubota, and T. Taniguchi, Synchronization and chaos in a spin-torque oscillator with a perpendicularly magnetized free layer, *Phys. Rev. B* **100**, 224422 (2019).
- [40] X. Wang and G. Chen, A chaotic system with only one stable equilibrium, *Commun. Nonlinear Sci. Numer. Simul.* **17**, 1264 (2012).
- [41] H. Yu, J. Chen, J. Wang, L. Sheng, H. Jia, W. Wei, H. Zhang, Y. Zhang, H. Wang, R. Yuan, S. Liu, T. Chen, D. Grundler, D. Yu, and J.-P. Ansermet, Deterministic switching of antiferromagnetic spin textures by chaotic magnons, <https://www.researchsquare.com/article/rs-2839142/v1> (2023).
- [42] M. N. Baibich, J. M. Broto, A. Fert, F. N. Van Dau, F. Petroff, P. Etienne, G. Creuzet, A. Friederich, and J. Chazelas, Giant magnetoresistance of (001)Fe/(001)Cr magnetic superlattices, *Phys. Rev. Lett.* **61**, 2472 (1988).
- [43] W. Kang, Y. Huang, X. Zhang, Y. Zhou, and W. Zhao, Skyrmion-electronics: An overview and outlook, *Proc. IEEE* **104**, 2040 (2016).
- [44] Y. Dong, G. Zhao, Y. Ma, Z. Pan, and R. Wu, A novel image encryption scheme based on pseudo-random coupled map lattices with hybrid elementary cellular automata, *Inf. Sci.* **593**, 121 (2022).
- [45] T. A. Denton, G. A. Diamond, R. H. Helfant, S. Khan, and H. Karagueuzian, Fascinating rhythm: A primer on chaos theory and its application to cardiology, *Am. Heart J.* **120**, 1419 (1990).
- [46] W. Legrand, D. Maccariello, F. Ajejas, S. Collin, A. Vecchiola, K. Bouzehouane, N. Reyren, V. Cros, and A. Fert, Room-temperature stabilization of antiferromagnetic skyrmions in synthetic antiferromagnets, *Nat. Mater.* **19**, 34 (2020).
- [47] L. Shen, Y. Zhou, and K. Shen, Programmable skyrmion-based logic gates in a single nanotrack, *Phys. Rev. B* **107**, 054437 (2023).